Materials Today Communications 35 (2023) 106132

Contents lists available at ScienceDirect

Materials Today Communications

journal homepage: www.elsevier.com/locate/mtcomm

Deformation and failure processes of Na-montmorillonite under uniaxial compressive strain condition via molecular dynamic method

Dongbo Li [a], Guangzhou Li [a], Zhentao Bai [a], Zongfang Han [b,c,*], Wei Lu [a]

[a] School of Science, Xi'an University of Architecture and Technology, Xi'an 710055, China
[b] Key Laboratory for Mechanics in Fluid Solid Coupling Systems, Institute of Mechanics, Chinese Academy of Sciences, Beijing 100190, China
[c] Guangdong Aerospace Research Academy, Guangdong 511400, China

ARTICLE INFO

Keywords:
Montmorillonite
Molecular dynamic
Water content
Mechanical anisotropy
Compressive mechanical properties

ABSTRACT

It is crucial to understand the compressive mechanical properties of bentonite for nuclear waste burial engineering while existing theories and methods are difficult to predict the mechanical properties and failure mechanisms of hydrated montmorillonite in the small strain scope. The structural evolution and mechanical behavior of different hydrated montmorillonite under compressive strain had been investigated through molecular dynamics simulation. Results indicated that the characteristics of deformation and failure in three directions were as follows. Compression in the X-direction led to the bending of the clay mineral planes, and rapid crack nucleation causing brittle failure. Y-direction compression caused the orientation of the clay mineral to tilt, local chemical bonds broke and dislocations occurred. Z-direction deformation was characterized by interlaminar compression, then stacking of layers, disordered distribution of atoms, and finally the collapse of the structural system. The mechanical properties of montmorillonite had a strong dependence on water content. There was a negative correlation between the ultimate compressive strength, Young's modulus, and water content in the X- and Y-directions. Meanwhile the bilayer hydrated state had a higher ultimate compressive strength than the other two ones in the Z-direction.

1. Introduction

Nuclear waste is rich in radioactive nuclides with extremely toxic and long half-life, so it needs to be properly processed, sealed and safely stored, which safe disposal is a major problem in the world. At present, the acceptable engineering scheme is deep geological burial, that is, high-level nuclear waste is sealed in geological bodies about 500–1000 m away from the surface [1].

The final deep geological disposal scheme of high-level radioactive waste in China is a multi-specific pathogen free deep geological disposal mode, and the buffer/backfill material is the last engineering barrier in the multi-specific pathogen free of high-level radioactive waste deep geological disposal repository [2].

Montmorillonite, the main clay mineral component of bentonite, has many advantages such as low permeability, low ion diffusion ability and good self-sealing ability, and has become a widely recognized engineering buffer/backfill material at home and abroad. It is of great significance to study the mechanical properties of bentonite, a buffer/backfill material in deep geological nuclear waste repository, for the safety evaluation and design of deep geological disposal of high-level radioactive waste [3].

Up to now, a large number of experimental tests and theoretical derivation methods have been used to study the structural characteristics and mechanical behavior of clay minerals [4–7], such as the Brillouin scattering method [8], nanoindentation test [9], and in-situ test [10]. The previous results showed that the mechanical properties of clay minerals were highly sensitive to water content and found obvious anisotropy in deformation and failure modes. At the same time, it was controlled by the local movement of clay aggregates at different scales [11]. Therefore, in the case of clay minerals, the molecular-level understanding of the clay mineral-water system interaction played an important role in the development of their microstructural evolution and multiscale modeling calculations.

The research methods of nano-mechanical behavior of clay minerals mainly include the first-principles and molecular dynamics (MD). First-principles can detect mechanical parameters such as elastic constants

* Correspondence to: Key Laboratory for Mechanics in Fluid Solid Coupling Systems, Institute of Mechanics, Chinese Academy of Sciences, Hai Dian, Beijing 100190, China.
E-mail address: hanzongfang@imech.ac.cn (Z. Han).

https://doi.org/10.1016/j.mtcomm.2023.106132
Received 23 March 2023; Received in revised form 26 April 2023; Accepted 4 May 2023
Available online 6 May 2023

and bulk modulus of clay minerals and the simulation results are convincing and reliable [12,13], but the number of atoms in the system that can be studied is very limited due to the heavy computational loading (not more than 100 atoms). The molecular dynamics method has the advantages of fast calculation speed, simulation of millions of atomic systems, and visual observation of the evolution process of clay mineral deformation and failure [14].

Therefore, molecular dynamics simulation was widely used to study the structural properties and nano-mechanical behavior of clay minerals, such as montmorillonite [15], illite [16], kaolinite [17], muscovite [18], etc. Schmidt et al. [19] used steered molecular dynamics to study the evolution of interlayer stress of Na-montmorillonite with hydration degree. It was found that the response of interlayer stress with deformation was linear in dehydration and single hydration state, but it became nonlinear with the increase of hydration degree. Carrier et al. [20] applied Voigt-Reuss-Hill (VRH) approximation method to estimate the macroscopic elastic properties of isotropic clay matrix and obtained the variation law of bulk and shear modulus with water content. Results showed that as the increase in water content, both bulk and shear modulus found a decreasing trend.

In the recent three years, Zhang et al. [21] explored the mechanical behavior of dehydrated kaolinite under uniaxial tension and compression in three directions(X, Y and Z). Yang et al. [14,22] further studied the influence of water content and temperature on the tensile mechanical properties of kaolinite. Furthermore, Zhu et al. [11] used molecular dynamics simulation to explore the compressive mechanical behavior of dehydrated montmorillonite under different loading paths and directions but did not consider the water content. Zhang et al. [23] utilized micro-indentation and mini-compression tests to investigate the effects of different water content and structural anisotropy on the mechanical properties of clay rock. Meanwhile, Wei et al. [24] explored the response discipline of water content and structural anisotropy to the tensile mechanical behavior of montmorillonite using molecular dynamics simulation.

While numerous studies have been conducted around the nano-mechanical behavior of clay minerals, they were focused on the mechanical properties under tensile and temperature effect. In contrast, the main deposit mineral of bentonite, one of which is the montmorillonite water adsorption and structural anisotropy has limited knowledge in terms of compressive mechanical behavior. And existing theories and methods are difficult to predict the mechanical properties and failure mechanisms of hydrated montmorillonite in the small compressive strain scope.

This paper detected the deformation and failure mechanism of the montmorillonite-water system under compressive strain through molecular dynamics simulation and introduced the bond fracture judgment criterion based on the radial distribution function of atom pairs to describe the structural characteristics of the system before compressive loading. Finally, according to the stress-strain relationship under different water contents, the response laws of mechanical parameters such as ultimate compressive strength and Young's modulus of montmorillonite in three directions were further explored.

2. Simulation details

2.1. System setup and force field

The Wyoming montmorillonite is a 2:1 layered aluminosilicate clay mineral, with a "TOT" structure of two layers of silicon-oxygen tetrahedron sandwiched by one layer of the aluminum-oxygen octahedron. The unit cell of montmorillonite was derived from the X-ray powder diffraction experiment of Viani et al. [25] and the formula is $Na_{0.75}(Si_{7.75}Al_{0.25})(Al_{3.5}Mg_{0.5})O_{20}(OH)_4$. Isomorphic substitution of montmorillonite follows Lowenstein's rule: (1) Adjacent silicon and aluminum atoms can not be substituted at the same time. (2) One out of every eight Al^{3+} is replaced by Mg^{2+} in the octahedral sheet, and one out of every 32 Si^{4+} in the tetrahedral is replaced by Al^{3+}, where the substitution sites are randomly distributed in the upper and lower silicon-oxygen tetrahedral and the middle aluminum-oxygen octahedral.

The basal spacing of montmorillonite was adjusted from an initial 15 Å to 9.6, 11.0, 12.5, and 14 Å, as shown in Fig. 1(a) and (b), then 4:2:1 cell expansion and isomeric substitution are performed, and the random addition of 0、32、64、96 water molecules between the layers, corresponding to the system with water contents of 0% (dehydrated), 10% (one layer), 20% (two layers), 30% (three layers). Water molecules were distributed randomly in the interlayer space of montmorillonite, which the calculation formula is showed in Eq. (1).

$$w\% = \frac{m_{H_2O}}{m_{MMT}} \times 100\% \tag{1}$$

Where w is water content, and m_{H_2O} and m_{MMT} are represent relative molecular mass of water and montmorillonite respectively.

At last, the model was expanded by 8a× 4b× 4c, and the supercell model of 128 cells was constructed. The modeling process of the montmorillonite-water system was shown in Fig. 1.

CLAYFF force field was applied for this work [26], which had been widely used in the molecular dynamics simulation of the interaction between clay minerals and solution systems. The water molecules adopted the SPC model. The total potential energy of the system mainly includes bonding interaction and non-bonding interaction, which could be calculated by Eq. (2).

$$\begin{aligned} E_{total} &= E_{bond\ stretch} + E_{angle\ bond} + E_{Coul} + E_{VDM} \\ &= k_1\left(r_{ij} - r_0\right)^2 + k_2\left(\theta_{ijk} - \theta_0\right)^2 + \frac{e^2}{4\pi\varepsilon_0}\sum_{i\neq j}\frac{q_i q_j}{r_{ij}} + \sum_{i\neq j}\varepsilon_{ij}\left[\left(\frac{\sigma_{ij}}{r_{ij}}\right)^{12} - 2\left(\frac{\sigma_{ij}}{r_{ij}}\right)^{6}\right] \end{aligned} \tag{2}$$

Where k_1 and k_2 are the force constants, and r_0 and θ_0 represent the equilibrium bond length and angle; r_{ij} is the distance between atoms i and j, θ_{ijk} is the angle of atoms i, j, and k; q_i and q_j are the charges of atoms i and j, respectively; ε_0 is the dielectric constant; ε and σ are the size and energy parameters respectively. The LJ potential parameters of different atoms are obtained by geometric and arithmetic averages, as shown in Eqs. (3) and (4).

$$\varepsilon_{ij} = \sqrt{\varepsilon_i \varepsilon_j} \tag{3}$$

$$\sigma_{ij} = \frac{\sigma_i + \sigma_j}{2} \tag{4}$$

2.2. Structural relaxation and simulation details

MD simulations were performed by LAMMPS (Large-scale Atomic and Molecular Parallel Simulator) program and the Paracloud platform [27]. The periodic boundary conditions were applied in three directions. Lennard-Jones potential model calculated the van der Waals with the cut-off radius of 10 Å. The Verlet algorithm was used for the integral equation. The Ewald summation method was applied to calculate the long-range Coulomb electrostatic force. The accuracy was set to 1.0×10^{-6} with a cut-off radius of 8.5 Å. The energy minimization algorithm used the conjugate gradient method with energy and stress convergence criteria of 1.0×10^{-6} kcal/mol and 1.0×10^{-8} kcal/(mol•Å) respectively, and the maximum number of iteration steps were both set to 1000.

To keep the montmorillonite-water system in the lowest energy state, the system was equilibrated with the isothermal-isobaric (NPT) ensemble for 200 ps. The Nose-Hoover anisotropic thermostat and barostat were applied for controlling temperature and pressure, with a temperature of 300 K and pressure of 0.1 MPa. The simulation timestep was set to 1 fs. Equilibrium dynamic traces were obtained and the last 50 ps were employed in analyzing the lattice constants, total energy, and

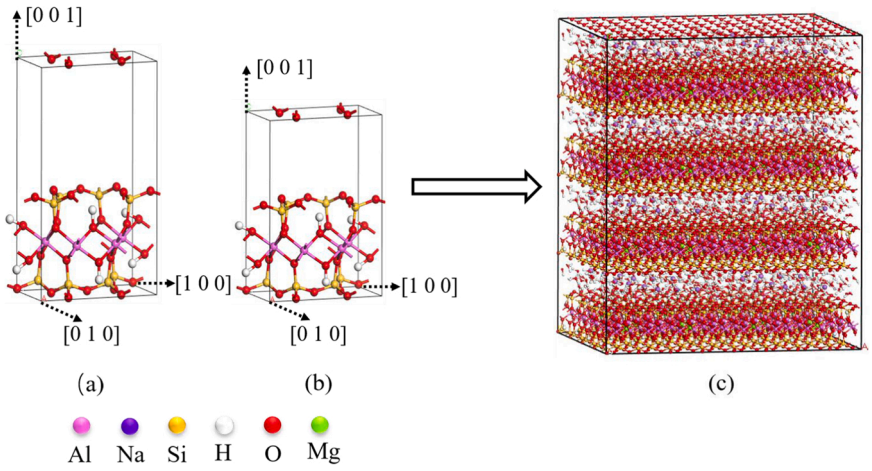

Fig. 1. Modeling process of hydrated Na-montmorillonite.

the basal spacing of montmorillonite at different water contents.

After the system reached equilibrium, uniaxial compression loading was performed along X, Y, and Z-directions (corresponding to the [1 0 0], [0 1 0], and [0 0 1] crystal orientation, respectively). Uniaxial compression simulations were achieved by changing the box size, which was called as strain-controlled loading method. The structural system was subjected to uniaxial compression along the X-direction by applying a certain compressive strain rate while maintaining the temperature and pressure at 300 K and 0.1 MPa in the Y- and Z-directions, respectively. Y- and Z-directions were simulated in uniaxial compression using the same approach.

To evaluate the effect of compressive strain rate on the mechanical properties of montmorillonite, referring to the simulation results of Wei et al. [24] and Yang et al. [14] and considering the consistency of control variables, the strain rates adopted in this paper were $10 \times 10–7\ fs^{-1}$, $8 \times 10–7\ fs^{-1}$, $5 \times 10–7\ fs^{-1}$ and $3 \times 10–7\ fs^{-1}$ respectively for uniaxial compression simulation to obtain a total strain of 0.3. The stress-strain curves during deformation and failure of montmorillonite in X-direction were showed in Fig. 2.

X-direction ultimate strain and maximum stress were not sensitive to the change in strain rate, and dehydrated montmorillonite coincided in the elastic stage under four different strain rates. It indicated that the compression rate was in the degree of $10^{-7}\ fs^{-1}$, even if slower three times, it would not greatly change the simulation results, which was consistent with the literature results of Zhang et al. [21] and Yang et al.

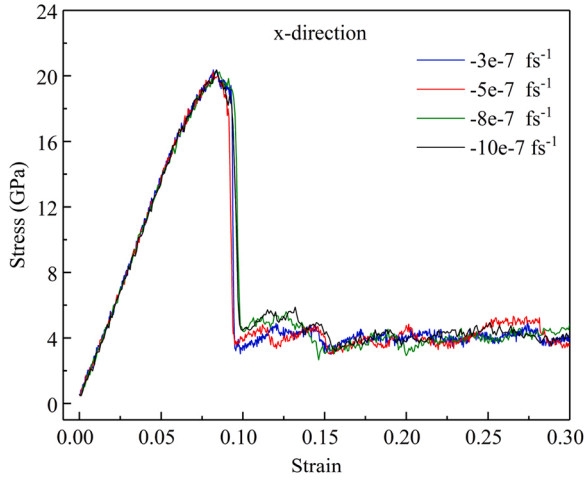

Fig. 2. Dehydrated montmorillonite of stress-strain curves under different strain rates.

[14]. Considering the accuracy of the simulation and saving computational resources, this paper selected the compression strain rate of $-5 \times 10^{-7}\ fs^{-1}$ to conduct the uniaxial compressive test for 600 ps to obtain a total strain of 0.3. In the process of uniaxial compression, the stress-strain relationship and displacement nephogram during deformation and failure were obtained.

3. Results and discussions

3.1. The atomic structure with different water contents before loading

The lattice parameters and total energy of Na-montmorillonite after relaxation at different water contents were showed in Table 1. The lattice parameters in the OA and OB directions did not change much with the increase in water contents, and the largest change occurred in the OC direction, which increased almost linearly. It indicated that the increase in volume was mainly caused by the change in OC direction. The total energy of the structure decreased with the increase of interlayer water content because the interaction between interlayer cations and the clay platelet would consume some energy. The total time required for molecular dynamics simulation of montmorillonite with water content of 0%, 10%, 20% and 30% were 5 h and 18 min, 6 h and 4 min, 8 h and 2 min, 14 h and 3 min respectively.

The interlayer spacing of Na-montmorillonite rose with the increases in water content, as shown in Fig. 3, which indicated that montmorillonite had happened water swelling in different degrees. The basal spacing of montmorillonite was close to the values of previous references [24,31]. It was proved that the building model and using the CLAYFF force field were accurate and reliable.

To understand the effect of water content on the structure of montmorillonite, the radial distribution functions (RDF) of Al-Ob, Al-Oh, Si-Ob, and Ob-Hw were investigated at different water contents, as shown in Fig. 4. Where g(r) is the number of atomic pairs in the range r to r + dr, it can characterize the stacking state, order of atoms and the distance between each bond. With the increase of the first peak

Table 1
Lattice parameters and total energy of Na-montmorillonite in different water content.

Water content (%)	Lattice parameters (Å)			Total energy (Kcal/mol)
	OA	OB	OC	
0	41.497	35.969	38.453	-1245077.1
10	41.728	36.170	44.306	-1249144.1
20	41.801	36.233	50.436	-1252643.4
30	41.888	36.309	56.606	-1256788.6

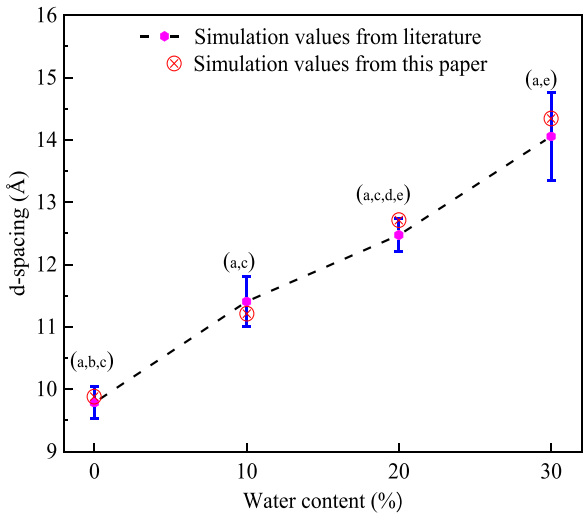

Fig. 3. The basal spacing of different hydrated montmorillonite (letters present references). a-[24]; b-[28]; c-[29]; d-[30]; e-[31].

intensity, the atoms were stacked more tightly, and the structure order was enhanced. The r corresponding to the first peak intensity could represent the bonding distance of the atomic pair.

In Fig. 4, the intensity of the first peaks in these RDF of Al-Ob, Al-Oh, and Si-Ob were positively correlated with water content. However, the position of the first peak that appeared at different water contents remained the same, which were 1.95, 1.93, and 1.57 Å respectively. It indicated that the increasing interlayer water content could make the atomic stack tighter, resulting in enhancing the interactive attraction between Al-Ob, Al-Oh, and Si-Ob atom pairs. While the intensity at the first peak of Ob-Hw decreased with the increasing water contents, which manifested that the interact attraction between the surface oxygen (Ob) of montmorillonite and water molecules was weakened at high water content. The analysis suggested that the increasing water contents could contribute to the basal spacing rising and montmorillonite swelling, which led to the weakening of the interact attraction between Ob-Hw.

Yang et al. proposed a bond-breakage criterion based on RDF, which considered the minimum distance corresponding to the intensity of the first peak of these RDF to be 0 as the position where the bond started to break [14]. At this point, the interaction force between atomic pairs was 0. It could be assumed that once the distance between pairs of atoms was perturbed by external strain greater than the distance, the bond would break. The above bond-breakage criteria can be applied to illustrate the structure properties of hydrated montmorillonite for the bonding of atomic pairs before loading. In the CLAYFF force field, only the covalent bonds such as hydroxyl bond and H-O-H between water molecules were considered, and interactions among other atoms were used for non-bonding. As a distinction, in the clay-water system, the bonding between Al…Ob, Si…Ob, Al…Oh and Ob…Hw was represented by virtual bonds.

In Fig. 4, the cutoff distances for each virtual bond of Al…Ob, Al…Oh and Si…Ob was presented, which were 2.69, 2.63, and 1.85 Å, respectively. The values were close to the Al…Ob, Al…Oh and Si…Ob virtual bond cutoff distances of 2.65, 2.85, and 1.85 Å calculated by Wei et al. [24]. The reliability of the force field and the correctness of the bond fracture criteria were further verified. Furthermore, Ob-Hw can represent the interaction between clay surface and interlayer water molecules, and the positions corresponding to the intensity of the first peak

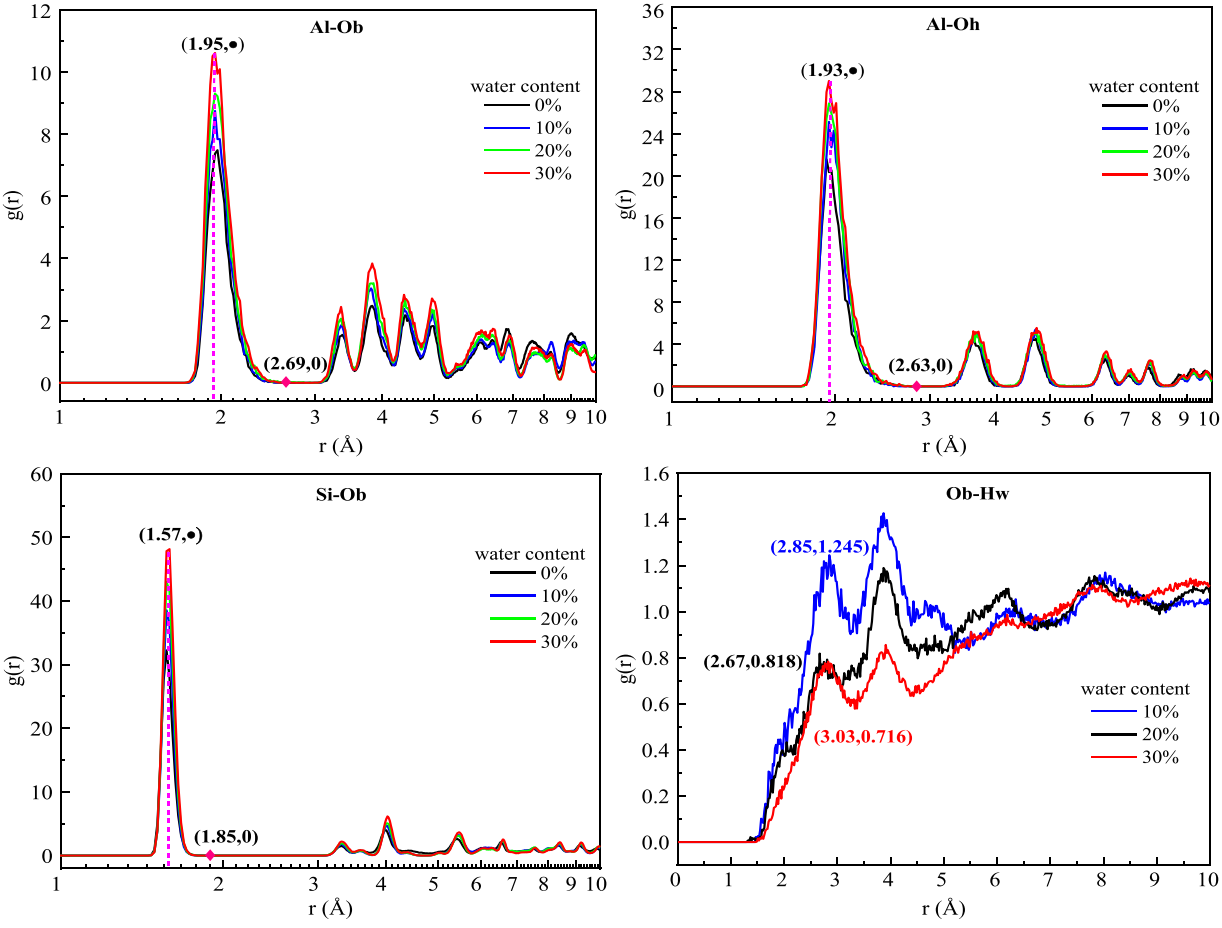

Fig. 4. Radial distribution functions of Al-Ob, Al-Oh, Si-Ob, and Ob-Hw with different water content.

with different water contents were 2.85, 2.67, and 3.03 Å, respectively. The maximum distance to form a hydrogen bond is 3.5 Å as determined by the definition of Lazur et al. [32]. It was evident that the oxygen atoms on the clay surface can form hydrogen bonds with water molecules. The hydrogen bonds formed between clay-Hw play an important role in the mechanical properties of montmorillonite.

3.2. Deformation and failure mechanism of the hydrated montmorillonite

3.2.1. Stress-strain relationship under uniaxial compression

Studying the stress-strain relationship of the clay-water system from a microscopic perspective is crucial to building predictive hydromechanical microscopic constitutive laws in a bottom-up approach. The stress-strain relationship obtained by uniaxial compression tests along X-, Y-, and Z-directions for different hydrated montmorillonites were shown in Fig. 5.

The process of deformation and failure was divided into three stages (1) elastic deformation stage OA (2) fracture deformation stage AB (3) failure deformation stage BD. Where the O point refers to the initial state under the started strain with 0. Point A is the peak stress, point B presents the position of the steep drop from the peak stress to the lowest point, and points C and D correspond to the deformation state at strain 0.15 and 0.2, respectively. The elastic deformation stage was characterized by a linear increase in stress with strain where the material could resist deformation at this stage.

With further compression, the strain continued to increase but stress decreased, indicating that the montmorillonite entered the fracture deformation stage. Last but not least, no matter how the strain increased, the stress was in a small range of fluctuations near the stable value, it was considered to be in the stage of failure deformation.

In Fig. 5(a), the stress increased linearly with strain from an initial state (O) to the peak stress (A) during compression of the hydrated montmorillonite along the X-direction. However, the slope of the stress-strain curve was distinct with different water contents, and the slope of the curve was smaller for higher water content, which suggested that interlayer water significantly reduced the stiffness of montmorillonite in the *x*-direction and the material's ability to resist elastic deformation was weakened. Thereafter, there was a sharp and steep drop from the peak stress (point A) to a relative minimum (B), when the number of strain changes was small but stress reduction was large, which indicated a sudden brittle failure to the structure.

Points O to A (Fig. 5b) had a linear growth zone similar to compression along the Y-direction and the slope decreased with increasing water contents, knowing that enhancing water contents weakened the stiffness in the Y-direction of montmorillonite. During the process from point A to B, the hydration of montmorillonite enhanced and the strain continues to increase but the stress decrease appeared in a flat segment, which meant that the montmorillonite underwent plastic deformation along the Y-direction, and it could characterize the ability of the material to withstand impact.

The compressive mechanical behavior of montmorillonite in the Z-direction showed nonlinearity and it was linear at small strain ($\varepsilon_{0-0.065}$)

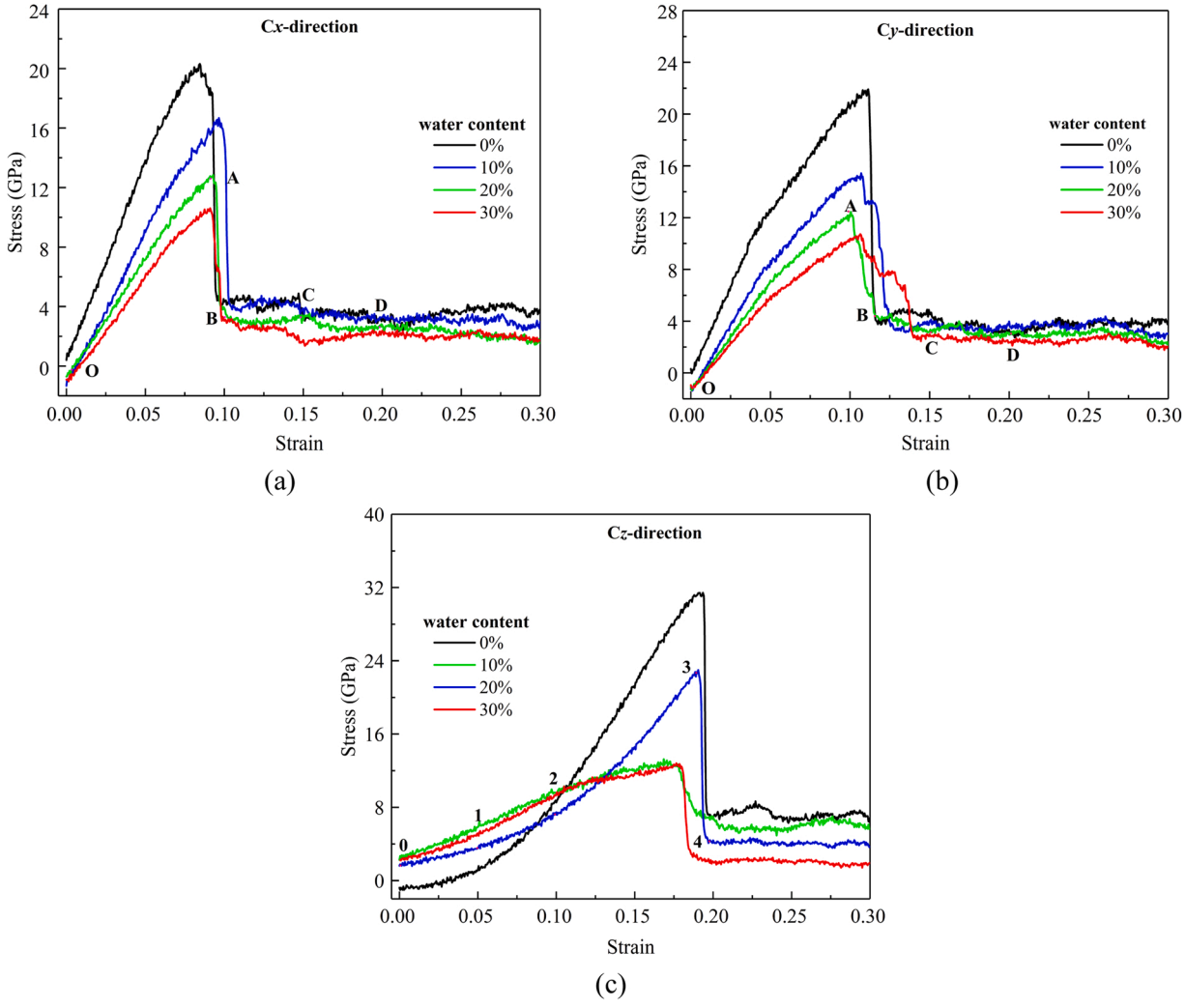

Fig. 5. Stress-strain curves of Na-montmorillonite with different water contents along three directions (*x*, *y* and *z*).

after the beginning of loading (Fig. 5c), which manifested that montmorillonite had elastic mechanical properties in this state. After linearity it became a nonlinear phase, increasing with strain until the peak stress was reached.

However, montmorillonite exhibited distinct mechanical behaviors in different hydration states, with the bilayer hydration montmorillonite showing higher peak stress than monolayer hydration. Montmorillonite in the monolayer and trilayer hydration state peak stress decrease trend was similar, and the stress drop was slow, meaning that monolayer and trilayer hydration montmorillonite had obvious ductile mechanical characteristics. These simulation results did not agree well with the conclusions obtained from previous experiments.

To further understand the special mechanical behavior of bilayer hydrated montmorillonite, Zhu et al. [33] investigated the atomic configuration of montmorillonite for different hydration states at peak stress. The deformation of montmorillonite could be described as interlayer domain compression, slight bending of clay planes, and disordered atomic arrangement, leading to the complete collapse of the structure. Especially in the monolayer hydration state was the most obvious, the structural deformation in the system was the most serious, leading to the peak stress in the monolayer hydration state being lower than the bilayer hydration. It can be concluded that the special mechanical behavior of bilayer hydrated montmorillonite was mainly attributed to the stable evolution of clay-solution interaction and deformation mode.

As mentioned above, the peak stress decreased with enhancing water content in the X- and Y-directions, and the maximum drop occurred at 10% water content. In the Z-direction, the variation pattern of peak stress with water content was not as obvious as in the X- and Y-directions, especially at a water content of 20%. This was mainly attributed to the difference in the deformation characteristics of clay platelet. In conclusion, the presence of interlayer water reduced the deformation resistance of montmorillonite, which was one of the critical factors for water adsorption and softening of soft rocks to induce large deformation and collapse.

3.2.2. *Analysis of structural deformation during compression*

The microscopic evolution pattern of deformation and failure for hydrated montmorillonite under uniaxial compressive strain was presented visually, which helped to understand the above stress-strain relationship. Since the deformation and failure patterns of montmorillonite were similar under four different water contents, the montmorillonite with 20% water content was selected for analysis, and the displacement clouds during deformation are shown in Fig. 6.

During compression, the atoms of hydrated montmorillonite were colored according to their displacement, and the color shades could represent the magnitude of the atomic motion displacement. In the strained state at point A in Fig. 6(a), the atomic displacement decreased from the boundary to the interior along the Z-direction, which still maintained the crystal structure, corresponding to the elastic phase of the OA in Fig. 5(a). With the accumulation of compressive strain, the clay layer produced buckling in the point B state, and the rapid expansion of cracks led to a sharp drop in stress. The strain accumulated from point C to D, the bending expands further, and the crack extends to reach the final failure mode.

In the stress at point B in Fig. 6(b), the crystal structure showed obvious deformation failure, but the clay layer orientation of the fracture failure mode was different from the X-direction. The clay platelet was observed to be tilted, with localized chemical bond breaks and obvious dislocations. However, in the strain state after point B, the movement of interlayer water molecules in the montmorillonite slit was more violent. In Fig. 6(c), during the gradual compression, the basal spacing of montmorillonite decreased, and the interlayer pore space disappeared, followed by the stacking of clay layers and the squeezing of water molecules into the clay layers. Continued compression of the structure produced deformation failure and more water molecules

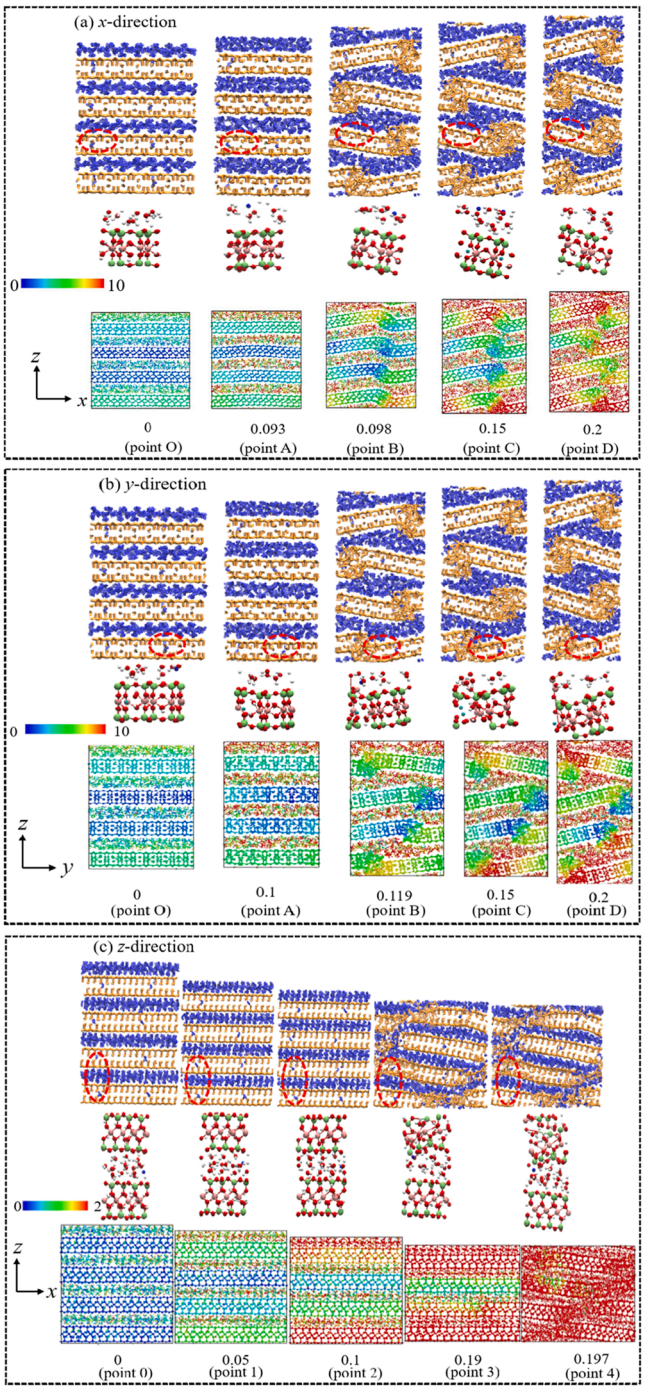

Fig. 6. The corresponding microstructures and strain cloud maps of Na-montmorillonite with the water content of 20% along *x*-, *y*- and *z*-directions.

entered the crystal structure, and the entering water molecules could weaken the bonding ability of the clay layer, leading to a reduction in the peak stress of montmorillonite.

3.3. *Compression mechanical parameters*

Ultimate compressive strength and ultimate compressive strain are the peak stress on the stress-strain curve and its corresponding strain. From the stress-strain relationships of Na-montmorillonite along the three directions at different water contents in Fig. 5, it could be seen that after the strain of 0.2, the stress no longer rise with the increase of strain, but kept fluctuating slightly around a certain fixed value. To ensure the

reliability of the residual compressive strength, we took the stress at strain 0.3 as the final residual compressive strength [24]. Young's modulus was obtained by the slope of the linear elastic state in a small strain range, where the selected strain ranges in three directions are: $\varepsilon_x = 0.06$, $\varepsilon_y = 0.05$, and $\varepsilon_z = 0.065$. Based on the ultimate compressive strength in three directions (X, Y and Z), the overall ultimate compressive strength can be calculated. Computed by Eq. (5).

$$\sigma_{\text{coverall}} = \sqrt{\frac{\sigma_{cx}{}^2 + \sigma_{cy}{}^2 + \sigma_{cz}{}^2}{3}} \tag{5}$$

To illustrate the post-peak intensity attenuation behavior of the hydrated montmorillonite, Peng et al. [34] proposed the intensity attenuation coefficient (Ds), which could be expressed as:

$$D_s = \frac{\sigma_c - \sigma_r}{\sigma_c} \tag{6}$$

Where σ_c represents ultimate compressive strength, and σ_r represents the residual compressive strength. The residual compressive strength, intensity attenuation coefficient, and overall ultimate compressive strength of montmorillonite along three directions (X, Y and Z) with different water contents were shown in Table 2.

The ultimate compressive strength and Young's modulus were illustrated in Fig. 7. In this paper, the ultimate compressive strength of dehydrated Na-montmorillonite in the X, Y and Z directions were 20 GPa, 22 GPa and 32 GPa, respectively, while the simulation values of Han et al. [35] were 21 GPa, 22 GPa and 34 GPa, respectively. By comparing them, it was found that the relative errors were 5%, 0% and 6.25%, which showed that the simulation results in this paper were consistent with those in previous literatures. The result of Young's modulus for dehydrated montmorillonite along the Z-direction was 55.116 GPa, while the values measured by Han et al. [35] and Katti et al. [36] were 54.56 GPa and 54.96 GPa, respectively. The comparison found that the results of this paper were similar to those of previous studies, confirming the reliability and correctness of the model and force field.

The ultimate compressive strength and Young's modulus of montmorillonite in the X- and Y-directions decreased with increasing water content, which indicated that interlayer water can reduce the strength and stiffness of montmorillonite. The ultimate compressive strength of montmorillonite along the Z-direction decreased linearly with 0%, 10%, and 30% water content, but a significant hysteresis occurred to 20% water content. Young's modulus showed obvious fluctuations at four different water contents, implying that the stiffness of montmorillonite along the Z-direction was sensitive to changes in water content. This was mainly attributed to the random distribution of water molecules in the interlayer space of montmorillonite and the interaction of the hydroxyl and silica layers with the water molecule. It further provided evidence for the anisotropy of mechanical properties of montmorillonite.

The residual compressive strength of hydrated Na-montmorillonite had a capacity of Z > Y>X in three directions, indicating that montmorillonite had the strongest resistance to damage in the Z-direction. It was why compression in the Z-direction led to a decrease in the basal spacing of montmorillonite, enhancing the van der Waals and Coulomb forces between the crystal layers, and an increase in the non-bonding interaction forces. Even though the structure was broken, there was still some resistance to deformation.

The intensity attenuation coefficient can reflect the capacity and mode of failure to some extent. The maximum intensity attenuation coefficient was 0.881 in all cases (corresponding to the state with 20% water content along the X-direction). From the stress-strain relationship in Fig. 5, it was clear that an abrupt brittle failure occurred in this state. While the minimum strength decay coefficient was 0.575 (corresponding to 10% water content along the Z-direction), and a gentle transition phase occurred at the peak stress and the turning point, which can be assumed that montmorillonite had some ductility and plastic failure occurred in this state.

4. Conclusions

Molecular dynamic simulations have been applied to study the effect of water content and structural anisotropy on atomic structure and compression mechanical properties of montmorillonite in three directions. The following conclusions were obtained:

(1) Since the CLAYFF force field could not describe the formation and breakage of bonds between atoms, a bond-breakage criterion based on the radial distribution function of atomic pairs was introduced to describe the structural properties of montmorillonite in terms of bond formation before loading. This bond breakage criterion could be applied to other clay minerals and crystal structures.
(2) The basal spacing of hydrated montmorillonite were consistent with the previous simulation results. The effect of water content on the RDF of Al-Ob, Al-Oh, and Si-Ob was as follows: increasing the water content can enhance the intensity of the first peak of RDF, but it had little effect on the position of the first peak.
(3) When compressed along the X and Y-directions, there were differences in the deformation and failure modes of hydrated montmorillonite. There was a bending of the clay mineral layer and fracture of chemical bonds locally, resulting in the brittle failure in the X-direction. While for the clay layer in the Y-direction, there was a certain inclination and dislocation at the fracture. Deformation features of the structure in the Z-direction can be described as interlayer compression, slight bending of the clay layer, and disorder of atomic arrangement, which eventually led to the complete collapse.
(4) The interlayer water remarkably decreased the ultimate compressive strength and Young's modulus of montmorillonite in the X- and Y-directions. The hydration of montmorillonite led to the reduction of strength and stiffness. At high water content (30%), the ability of water molecules to invade montmorillonite crystals was enhanced, and the deformation and damage were more severe when disturbed by external compressive strain. The above fully demonstrated that montmorillonite had obvious anisotropic properties.

CRediT authorship contribution statement

Dongbo Li: Conceptualization, Methodology, Investigation, Writing – review & editing, Supervision, Project administration. **Guangzhou Li:**

Table 2
Residual compressive strength, intensity attenuation coefficient, and overall compressive strength of different hydrated montmorillonite.

Water content (%)	Residual compressive strength (GPa)			Intensity attenuation coefficient			Overall compressive strength (GPa)
	x	*y*	*z*	*x*	*y*	*z*	
0	3.562	3.732	6.888	0.825	0.829	0.781	25.031
10	2.993	3.058	5.634	0.821	0.799	0.575	15.119
20	1.534	2.146	3.711	0.881	0.827	0.839	16.823
30	1.693	2.008	1.912	0.841	0.813	0.851	11.432

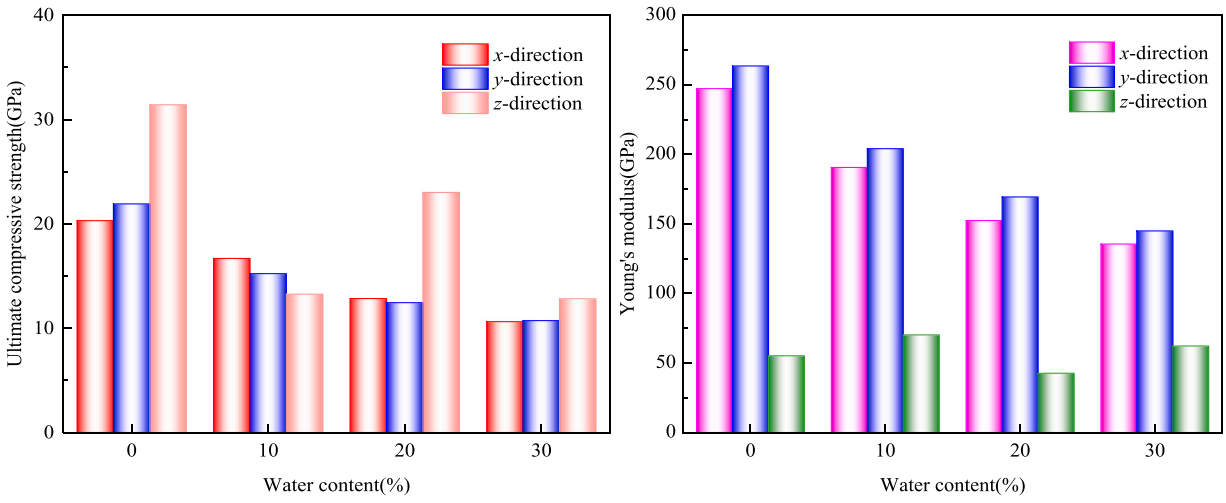

(a) Ultimate compressive strength (b) Young's modulus

Fig. 7. Evolution of compressive mechanical parameters with water content for montmorillonite along three directions.

Conceptualization, Data curation, Writing – review & editing. **Zhentao Bai:** Methodology, Software Visualization. **Zongfang Han:** Supervision, Writing – review & editing. **Wei Lu:** Project administration.

Declaration of Competing Interest

The authors declare that they have no known competing financial interests or personal relationships that could have appeared to influence the work reported in this paper.

Data Availability

The data that has been used is confidential.

Acknowledgments

This work was supported by the General program of the National Natural Science Foundation of China (51878547), National Natural Science Foundation of China Youth Science Fund (52008332), China Postdoctoral Fund Regional Special Support Program (2021M693877), the Guangdong Aerospace Research Academy Research Project (GARA2022003000), and the Experiments for Space Exploration Program and the Qian Xuesen Laboratory, China Academy of Space Technology (TKTSPY-2020-05-01).

References

[1] R. Pusch, 2008. Geological storage of highly radioactive waste, current concepts and plans for radioactive waste disposal, Springer -Verlag Berlin Heidelberg. (2008).
[2] C.L. Zhang, J. Wang, K. Su, Concepts and tests for disposal of radioactive waste in deep geological formations, Chin. J. Rock Mech. Eng. 25 (4) (2006) 750–767.
[3] W. Yang, R.P. Chen, X. Kang, Z. Ali, Radionuclide adsorption mechanism in buffer materials in high-level radioactive waste container: MD study, Chin. J. Geotech. Eng. 42 (2) (2020) 240–245.
[4] S. Hedan, F. Hubert, D. Prêt, F. Eric, V. Valéry, Measurement of the elastic properties of swelling clay minerals using the digital image correlation method on a single macroscopic crystal, Appl. Clay Sci. 117 (2015) 248–256.
[5] N.H. Mondol, J. Jahren, K. Bjørlykke, Elastic properties of clay minerals, Lead. Edge. 27 (2008) 758–770.
[6] B. Chen, J.R.G. Evans, Elastic moduli of clay platelets, Scr. Mater. 54 (2006) 1581–1585.
[7] J.A. Ortega, F.J. Ulm, Y. Abousleiman, The effect of the nanogranular nature of shale on their poroelastic behavior, Acta Geotech. 2 (2007) 155–182.
[8] L.E. McNeil, M. Grimsditch, Elastic moduli of muscovite mica, J. Phys. Condens. Matter 5 (1993) 1681–1690.
[9] Y. Wu, Y. Li, S. Luo, Multiscale elastic anisotropy of a shale characterized by cross-scale big data nanoindentation, Int. J. Rock. Mech. Min. Sci. 134 (2020), 104458.
[10] T. Húlan, A. Trník, I. Štubňa, P. Bačík, Development of Young's modulus of illitic clay during heating up to 1100 °C, Mater. Sci. 21 (3) (2015) 429–434.
[11] L. Zhu, W. Shen, J. Shao, Insight of molecular simulation to better assess deformation and failure of clay-rich rocks in compression and extension, Int. J. Rock Mech. Min. Sci. 138 (2021), 104589.
[12] C.M. Moy, G.O. Seltzer, D.T. Rodbell, Variability of El nino/southern oscillation activity at millennial timescales during the Holocene epoch, Nature 420 (2002) 162–165.
[13] B. Militzer, H.R. Wenk, S. Stackhouse, First-principles calculation of the elastic moduli of sheet silicates and their application to shale anisotropy, Am. Mineral. 96 (2010) 125–137.
[14] H. Yang, M. He, C. Lu, Deformation and failure processes of kaolinite under tension: insights from molecular dynamics simulations, Sci. China Phys. Mech. Astron. 62 (2019), 064612.
[15] D. Ebrahimi, R.J. Pellenq, A.J. Whittle, Nanoscale elastic properties of montmorillonite upon water adsorption, Langmuir 28 (2012) 16855–16863.
[16] G. Hantal, L. Brochard, H. Laubie, et al., Atomic-scale modelling of elastic and failure properties of clays, Mol. Phys. 112 (2014) 1294–1305.
[17] B.K. Benazzouz, A. Zaoui, A nanoscale simulation study of the elastic behaviour in kaolinite clay under pressure, Mater. Chem. Phys. 132 (2012) 880–888.
[18] S.L. Teich-McGoldrick, J.A. Greathouse, R.T. Cygan, Molecular dynamics simulations of structural and mechanical properties of muscovite: pressure and temperature effects, J. Phys. Chem. C 116 (2012) 15099–15107.
[19] S.R. Schmidt, D.R. Katti, P. Ghosh, Evolution of mechanical response of sodium montmorillonite interlayer with increasing hydration by molecular dynamics, Langmuir 21 (2005) 8069–8076.
[20] B. Carrier, M. Vandamme, R.J.M. Pellenq, V.D. Henri, Elastic properties of swelling clay particles at finite temperature upon hydration, J. Phys. Chem. C 118 (2014) 8933–8943.
[21] L.L. Zhang, Y.Y. Zheng, P.C. Wei, Q.F. Diao, Nanoscale mechanical behavior of kaolinite under uniaxial strain conditions, Appl. Clay Sci. 201 (2021), 105961.
[22] Z.F. Han, H. Yang, M.C. He, A molecular dynamics study on the structural and mechanical properties of hydrated kaolinite system under tension, Mater. Res. Expr. 6 (2019) 0850c3..
[23] F. Zhang, S.Y. Xie, D.W. Hu, J.F. Shao, Effect of water content and structural anisotropy on mechanical property of claystone, Appl. Clay Sci. 69 (2012) 79–86.
[24] P.C. Wei, Y.Y. Zheng, Y. Xiong, S.B. Zhou, Effect of water content and structural anisotropy on tensile mechanical properties of montmorillonite using molecular dynamics, Appl. Clay Sci. 228 (2022), 106622.
[25] A. Viani, A.F. Gualtieri, G. Artioli, The nature of disorder in montmorillonite by simulation of X-ray powder patterns, Am. Mineral. 87 (2002) 966–975.
[26] R.T. Cygan, J.-J. Liang, A.G. Kalinichev, Molecular models of hydroxide, oxyhydroxide, and clay phases and the development of a general force field, J. Phys. Chem. B 108 (2004) 1255–1266.
[27] A.P. Thompson, H.M. Aktulga, R. Berger, D.S. Bolintineanu, LAMMPS - a flexible simulation tool for particle-based materials modeling at the atomic, meso, and continuum scales, Comput. Phys. Commun. 271 (2022), 108171.
[28] L.F. Kuang, G. Zhou, X. Shang, Molecular dynamic simulation of interlayer water structure in Na-montmorillonite, J. China Coal Soc. 38 (2013) 418–423.
[29] M. Chávez-Páez, K. Van Workum, L. de Pablo, Monte Carlo simulations of Wyoming sodium montmorillonite hydrates, J. Chem. Phys. 114 (2001) 1405–1413.
[30] F.R.C. Chang, N.T. Skipper, G. Sposito, Computer simulation of interlayer molecular structure in sodium montmorillonite hydrates, Langmuir 11 (2002) 2734–2741.
[31] G. Kosakowski, S.V. Churakov, T. Thoenen, Diffusion of Na and Cs in montmorillonite, Clays Clay Miner. 56 (2008) 190–206.

[32] A. Luzar, D. Chandler, Hydrogen-bond kinetics in liquid water, Nature 379 (1996) 55–57.
[33] L.P. Zhu, W.Q. Shen, M.C. He, J.F. Shao, Contribution of atomistic study to better understand water saturation effect on mechanical behavior of clayey rocks in triaxial compression, Comput. Geotech. 146 (2022), 104738.
[34] J. Peng, G. Rong, M. Cai, K. Peng, Determination of residual strength of rocks by a brittle index, Rock. Soil Mech. 36 (2015) 403–408.
[35] Z.F. Han, H. Yang, M. Bu, M.C. He, A molecular dynamics study on the structural and mechanical properties of pyrophyllite and M-Montmorillonites (M = Na, K, Ca, and Ba), Chem. Phys. Lett. 803 (2022), 139848.
[36] D.R. Katti, S.R. Schmidt, P. Ghosh, K.S. Katti, Modeling the response of pyrophyllite interlayer to applied stress using steered molecular dynamics, Clays Clay Miner. 53 (2) (2005) 171–178.